Article

Diagnosis of Reverse-Connection Defects in High-Voltage Cable Cross-Bonded Grounding System Based on ARO-SVM

Yuhao Ai [1,2], Bin Song [1,2,*], Shaocheng Wu [1,2], Yongwen Li [1,2], Li Lu [1,2] and Linong Wang [1,2]

1 Hubei Key Laboratory of Power Equipment & System Security for Integrated Energy, School of Electrical Engineering and Automation, Wuhan University, Wuhan 430072, China; 2023282070150@whu.edu.cn (Y.A.); wushaocheng@whu.edu.cn (S.W.); 2024282070189@whu.edu.cn (Y.L.); luli_ee@whu.edu.cn (L.L.); wangln@whu.edu.cn (L.W.)
2 School of Electrical Engineering and Automation, Wuhan University, Wuhan 430072, China
* Correspondence: binsong@whu.edu.cn; Tel.: +86-136-5723-6456

Abstract: High-voltage (HV) cables are increasingly used in urban power grids, and their safe operation is critical to grid stability. Previous studies have analyzed various defects, including the open circuit in the sheath loop, the flooding in the cross-bonded link box, and the sheath grounding fault. However, there is a paucity of research on the defect of the reverse direction between the inner core and the outer shield of the coaxial cable. Firstly, this paper performed a theoretical analysis of the sheath current in the reversed-connection state and established a simulation model for verification. The outcomes of the simulation demonstrate that there are significant variations in the amplitudes of the sheath current under different reversed-connection conditions. Consequently, a feature vector was devised based on the amplitude of the sheath current. The support vector machine (SVM) was then applied to diagnose the reversed-connection defects in the HV cable cross-bonded grounding system. The artificial rabbits optimization (ARO) algorithm was adopted to optimize the SVM model, attaining an impressively high diagnostic accuracy rate of 99.35%. The effectiveness and feasibility of the proposed algorithm are confirmed through the analysis and validation of the practical example.

Keywords: high-voltage cable; defect diagnosis; sheath current; ARO

1. Introduction

The scale of power transmission and distribution grids has been increasing year by year with the development of urbanization. HV cables are widely used due to their advantages, such as meeting the requirements of electric energy transmission and protecting the urban landscape, and their proportion in the power grid is becoming larger and larger [1,2]. Therefore, the safe operation of cables plays an irreplaceable role in ensuring the stability of the power grid [3–5].

Power grid workers usually refer to single-core coaxial cables with a rated working voltage of 110 kV and above as HV cables. During operation, the principle of electromagnetic induction states that an induced voltage will appear on the metal sheath of the cable [6]. This induced voltage will change due to the influence of the core current and the cable length. The metal shielding layer of HV cables can reduce the mutual influence between the internal and external electric fields. The grounding methods usually adopted include direct grounding, grounding at both ends, and cross-bonded grounding [7]. The use of cross-bonded grounding can effectively limit the excessive induced voltage and sheath current of HV cables. In the maintenance and inspection of the HV cable cross-bonded

grounding system, the sheath current is one of the important parameters reflecting the cable state. Based on the changes in the sheath current, cable fault states can be effectively diagnosed [8–10].

Damage to the sheath, incorrect wiring in link boxes, the puncture of epoxy prefabricated parts, and the reversal of the direction of the core and outer shielding layer of coaxial cables are all reasons that can cause changes in the sheath current of the HV cable cross-bonded grounding system, affecting the normal operation of the cables [11,12]. In identifying abnormal sheath currents in HV cable cross-bonded grounding systems, personnel are required to undertake a range of diagnostic procedures to ascertain the nature and location of cable faults. These include partial discharge monitoring [13], insulation resistance monitoring [14], grounding current monitoring [15], etc. This process can significantly impact the stability of the power system. Consequently, the expeditious diagnosis of cable fault types and the swift identification of fault locations are of paramount importance [16]. Scholars both domestically and internationally have conducted research and analysis in various directions regarding the cross-bonded grounding systems of HV cables. Reference [17] proposed a methodology for analyzing the cable sheath current, utilizing the separation of the cable sheath current and the resistive current from the leakage current to determine the presence of a cable fault. This approach was substantiated through the utilization of both simulation and experimental methods. However, it should be noted that the method is constrained in its capacity to analyze a wide range of cable faults, encompassing only cable insulation faults, cable sheath loop faults, and cable joint puncture faults. Reference [18] constructed a feature vector based on the amplitude and phase angle of the sheath current in the grounding boxes at both ends, and employed the long short-term memory (LSTM) algorithm to perform the intelligent classification of faults in the cable cross-bonded grounding system. However, in practical engineering, the phase angle of the sheath current was rarely used to assess cable faults, and the proposed method required verification. Reference [19] proposed a fault location method based on the electrical quantities at both cable ends. A substantial body of simulation results demonstrated the capability of this method to locate the fault starting point accurately. However, the data analysis of the proposed method was relatively complex. Reference [20] introduced the defect of the coaxial cable core and shielding direction being reversed, and analyzed its circulating current characteristics. Although it achieved the classification and generalization of common reversal defects, the leakage current was overlooked, only the induced current was considered, and it did not employ simulation for validation.

Current online detection methods for cable faults typically involve the construction of feature vectors based on a substantial number of feature quantities to facilitate the identification of faults. However, these methods are deficient in their coverage of fault types, particularly in the context of coaxial cable core and outer shielding layer reversals, a phenomenon that has received scant attention in the extant literature. When the connection direction between the cable core and the outer shielding layer is reversed, the circulating current in the sheath will increase significantly, leading to operational failures. This will further endanger the stability of the power system, potentially causing power outages and economic losses. Furthermore, the utilization of intelligent algorithms, such as machine learning and deep learning, in the field of cable fault diagnosis for cross-bonded grounding systems is also limited. Among them, due to its excellent classification performance, strong nonlinear processing ability, and high anti-interference capacity, the SVM has been widely applied in the field of fault diagnosis [21,22]. However, the selection of hyperparameters in the SVM directly affects the results of the fault diagnosis.

Therefore, this paper proposed a diagnosis method for reverse-connection defects in the cross-bonded grounding system of HV cables based on an optimized SVM algorithm. The main contributions of this paper were as follows:

1. The reverse-connection defects between the core and the outer shielding layer of coaxial cables were systematically integrated. The theoretical situations of sheath currents under different reverse-connection states were analyzed, providing theoretical guidance for grid workers to diagnose reverse-connection defects in the cable cross-bonded grounding system.

2. A simulation model of the cable cross-bonded grounding system was built using the Power System Computer-Aided Design (PSCAD) simulation software, version v4.6.2. The theoretical situations of sheath currents under different reverse-connection states were verified. It was found that the amplitude of the sheath current varied significantly under different operating conditions, providing a basis for the subsequent construction of feature vectors.

3. A feature vector based on the amplitude of the sheath current was constructed. The ARO algorithm optimized the SVM model and compared it with the particle swarm optimization (PSO) and sparrow search algorithm (SSA). This improved the accuracy and efficiency of multi-classification fault diagnosis, and the accuracy rate was increased by 5.84% compared with the basic model.

2. Analysis of Sheath Currents Under Normal Operation

In HV cable lines with a length greater than 1000 m, the metal sheath grounding system of HV cables generally employed a cross-bonded method to reduce the induced voltage and sheath current. The configuration of the HV cable cross-bonded grounding system was illustrated in Figure 1.
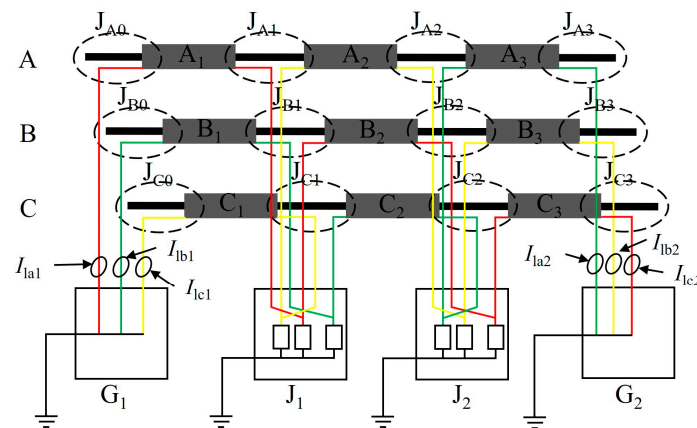
Figure 1. Model of cross-bonded grounding system for HV cables.

Figure 1 showed a cross-bonded main section, and a typical HV cable line generally consists of several such sections. Each main section contained two direct grounding boxes at the ends (G_1 and G_2), two cross-bonded grounding boxes (J_1 and J_2), nine minor metallic sheath sections of approximately equal length (A_1, A_2,…, C_3), and twelve cable joints (J_{A0}, J_{A1},…, J_{C3}). The sheath of the HV cable was transposed utilizing cross-bonded boxes, forming three sheath return loops: A_1-B_2-C_3, B_1-C_2-A_3, and C_1-A_2-B_3. The cable sheath currents, designated I_{la1}, I_{lb1}, I_{lc1}, I_{la2}, I_{lb2}, and I_{lc2}, could be divided into leakage currents [23] and sheath-induced currents. These sheath currents flowed directly to the earth through G_1 and G_2, completing the closed circuit.

2.1. Leakage Current

The flow direction of the leakage current of the cable was from the cable core through the insulating layer to the metal sheath. Taking minor section A_1 as an example for the introduction, its flow direction schematic diagram was shown in Figure 2.
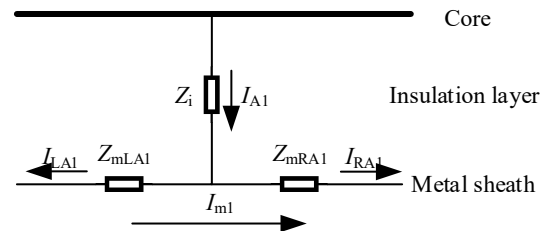
Figure 2. Schematic diagram of the flow direction of the leakage current of the cable in minor section A_1.

In Figure 2, I_{A1} represented the leakage current of the cable, while I_{LA1} and I_{RA1} were the components of the leakage current flowing to the left and right in the metal sheath, respectively. Their equivalent relationship could be seen in Equation (1). Z_i was the equivalent impedance of the insulating layer, and Z_{mLA1} and Z_{mRA1} were the equivalent impedances of the left and right sides of the cable metal sheath, respectively.

$$I_{A1} = I_{LA1} + I_{RA1} \tag{1}$$

$$Z_{mA1} = Z_{mLA1} + Z_{mRA1} \tag{2}$$

where Z_{mA1} was the equivalent impedance of the minor section A1 of the metal sheath.

Since the capacitive current accounted for a relatively large proportion of the leakage current, the leakage current was approximated as the capacitive current:

$$I_{A1} \approx I_{CA1} = jwCU_A l_{A1} \tag{3}$$

where I_{CA1} represented the capacitive current, U_A was the voltage of the cable core, l_{A1} was the length of the minor section A_1 of the metal sheath, and C was the capacitance of the cable with its value obtainable from Equation (4). Since the voltage of the HV cable cross-bonded grounding system and the impedance of the cable insulating layer would not change in a short period, the cable leakage current could be considered approximately constant.

$$C = \frac{\varepsilon_r \times 5.56 \times 10^{-11}}{\ln\left(\frac{D_C + 2\delta}{D_C}\right)} \tag{4}$$

where ε_r was the relative dielectric constant, D_C was the diameter of the cable core, and σ was the thickness of the insulator. The relative dielectric constant of the cross-linked polyethylene was 2.3.

The leakage current components in the sheath loop could be calculated according to the current distribution rule. Take section A_1 as an example—I_{LA1} and I_{RA1} could be obtained as follows:

$$\begin{cases} I_{LA1} = \frac{Z_{mRA1} + Z_{mB2} + Z_{mC3} + R_g}{Z_{mA1} + Z_{mB2} + Z_{mC3} + R_e + R_g} I_{A1} \\ I_{RA1} = \frac{Z_{mLA1} + R_e}{Z_{mA1} + Z_{mB2} + Z_{mC3} + R_e + R_g} I_{A1} \end{cases} \tag{5}$$

where Z_{mA1}, Z_{mB2}, and Z_{mC3} were the equivalent impedances of the three minor sections A_1, B_2, and C_3 of the metal sheath, respectively, and R_e and R_g were the grounding resistances at both ends of the cross-bonded loop.

2.2. Sheath-Induced Current

The current generated in the sheath loop based on the principle of electromagnetic induction was called the sheath-induced current. The equivalent induced circuit of the metal sheath of the cross-bonded cable was shown in Figure 3.
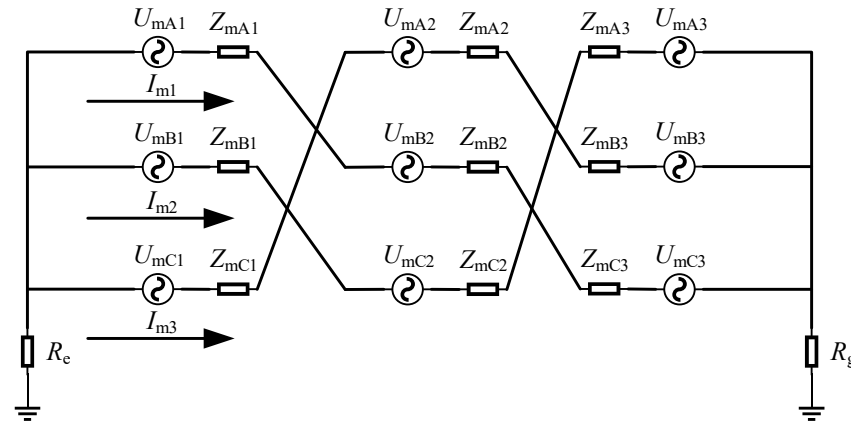
Figure 3. Equivalent induced circuit of the metal sheath of the cross-bonded cable.

In the figure, U_{mAn}, U_{mBn}, and U_{mCn} (n = 1, 2, 3) were the induced voltages of the metal sheaths of each section of the cable. Z_{mAn}, Z_{mBn}, and Z_{mCn} were the equivalent impedances of the metal sheaths of each section of the cable, respectively, and I_{m1}, I_{m2}, and I_{m3} were the induced circulating currents of the three sheath loops whose values can be calculated by Equation (6).

$$\begin{cases} I_{m1} = \frac{U_{mA1}+U_{mB2}+U_{mC3}}{Z_{mA1}+Z_{mB2}+Z_{mC3}+R_e+R_g} \\ I_{m2} = \frac{U_{mB1}+U_{mC2}+U_{mA3}}{Z_{mB1}+Z_{mC2}+Z_{mA3}+R_e+R_g} \\ I_{m3} = \frac{U_{mC1}+U_{mA2}+U_{mB3}}{Z_{mC1}+Z_{mA2}+Z_{mB3}+R_e+R_g} \end{cases} \tag{6}$$

Taking minor section A_1 as an example to calculate its induced voltage, the length of the HV cable, the method of installation, and the core current could all have an effect on the induced voltage of the sheath. However, since the induced current was much smaller than the core current, the effect of the sheath-induced current on the induced voltage was not considered. The calculation of its induced voltage was as follows:

$$U_{mA1} = -jw(I_A L_{AA} + I_B L_{AB} + I_C L_{AC})l_{A1} \tag{7}$$

where I_A, I_B, and I_C were the cable core currents of phases A, B, and C, respectively. L_{AA} was the mutual inductance coefficient of the core of phase A to the metal sheath of phase A, M_{AB} was the mutual inductance coefficient of the core of phase B to the metal sheath of phase A, and M_{AC} was the mutual inductance coefficient of the core of phase C to the metal sheath of phase A.

2.3. Current in the Grounding Boxes

The sheath current in the grounding boxes at both ends was the vector sum of the leakage current and the sheath induced current. This paper stipulated that the positive direction of the current flow is to the right. The change of the sheath current in the grounding box could reflect the operation status of the sheath loop. According to the above analysis, the sheath current in the grounding box was as shown in Equation (8). When ideal conditions such as the same cable laying method, equal lengths of cross-bonded sections, and balanced core load currents were met, the induced voltages on each section

of the metal sheath generally satisfied the following relationships—$U_{mA1} = U_{mA2} = U_{mA3}$, $U_{mB1} = U_{mB2} = U_{mB3}$, $U_{mC1} = U_{mC2} = U_{mC3}$—and the magnitudes of U_{mAn}, U_{mBn}, and U_{mCn} were equal. The amplitude when the three voltages were equal was designated U_m. The phase of U_{mAn} preceded the phase of U_{mBn} by 120°, and the phase of U_{mBn} succeeded the phase of U_{mCn} by 120°. It was evident that the magnitude and phase relationships of the voltages of each phase core were similar. Furthermore, the equivalent impedances of each section of the metal sheath were approximately equal. We denoted this by Z_m. It was evident that I_{m1}, I_{m2}, and I_{m3} were close to 0 when the cable functioned within normal parameters.

Consequently, when the cable functioned within normal parameters, the sheath current within the grounding enclosure was predominantly influenced by the leakage current.

$$\begin{cases} I_{la1} = -(I_{LA1} + I_{LB2} + I_{LC3}) + I_{m1} \\ I_{lb1} = -(I_{LB1} + I_{LC2} + I_{LA3}) + I_{m2} \\ I_{lc1} = -(I_{LC1} + I_{LA2} + I_{LB3}) + I_{m3} \\ I_{la2} = (I_{RB1} + I_{RC2} + I_{RA3}) + I_{m2} \\ I_{lb2} = (I_{RC1} + I_{RA2} + I_{RB3}) + I_{m3} \\ I_{lc2} = (I_{RA1} + I_{RB2} + I_{RC3}) + I_{m1} \end{cases} \tag{8}$$

where I_{la1} and I_{lc2} were the currents at the beginning and end of the sheath loop A$_1$-B$_2$-C$_3$, I_{lb1} and I_{la2} were the currents at the beginning and end of the sheath loop B$_1$-C$_2$-A$_3$, and I_{lc1} and I_{lb2} were the currents at the beginning and end of the sheath loop C$_1$-A$_2$-B$_3$.

3. Analysis of Sheath Currents for Reverse-Connection Defects

In a normal cross-bonded grounding system, the inner core and outer shielding layer of the grounded coaxial cable are connected to the aluminum sheath at the far and near ends, respectively. Typically, we designate the aluminum sheath along the direction of the coaxial cable as the proximal end, and the opposite end as the distal end, as illustrated in Figure 4. If there is a reverse-connection defect between the inner core and outer shielding layer of the coaxial cable, the induced voltage of the cable metal sheath cannot be canceled out. This results in an increase in the sheath current and a reduction in the service life of the insulation. The following analysis will examine the sheath current of the reverse-connection defect, focusing primarily on one reverse connection and two reverse connections. The specific reverse-connection defect states are shown in Table 1. Since the probability of three or more simultaneous reverse connections is extremely low, this paper does not consider it.
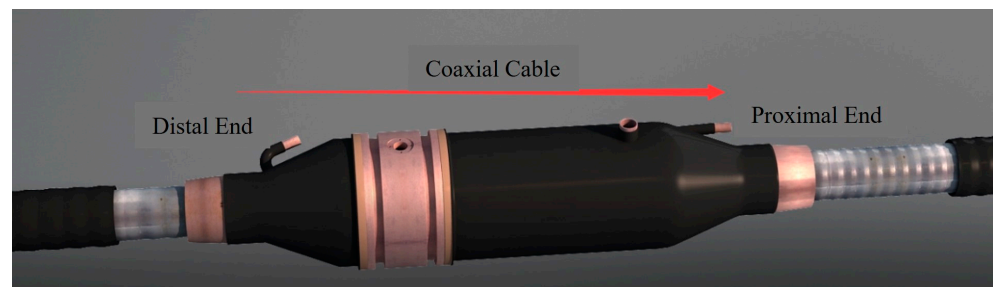
Figure 4. Schematic diagram of coaxial cable joint.

Table 1. Classification of states of HV cable cross-bonded grounding system.

Defect Type	Defect Location	State Number
Normal	/	0
A reversed connection in the cable joint	Misconnection of joint J_{A1}	1
	Misconnection of joint J_{B1}	2
	Misconnection of joint J_{C1}	3
	Misconnection of joint J_{A2}	4
	Misconnection of joint J_{B2}	5
	Misconnection of joint J_{C2}	6
Reversed connections in two cable joints	Misconnection of joint J_{A1} and J_{B1}	7
	Misconnection of joint J_{B1} and J_{C1}	8
	Misconnection of joint J_{C1} and J_{A1}	9
	Misconnection of joint J_{A2} and J_{B2}	10
	Misconnection of joint J_{B2} and J_{C2}	11
	Misconnection of joint J_{C2} and J_{A2}	12
	Misconnection of joint J_{A1} and J_{A2}	13
	Misconnection of joint J_{B1} and J_{B2}	14
	Misconnection of joint J_{C1} and J_{C2}	15
	Misconnection of joint J_{A1} and J_{B2}	16
	Misconnection of joint J_{B1} and J_{C2}	17
	Misconnection of joint J_{C1} and J_{A2}	18
	Misconnection of joint J_{B1} and J_{A2}	19
	Misconnection of joint J_{C1} and J_{B2}	20
	Misconnection of joint J_{A1} and J_{C2}	21

3.1. One Reversal

There was a total of six types of single-reversal defects where the inner core and outer shielding layer of the coaxial cable were reversed: J_{A1}, J_{B1}, J_{C1}, J_{A2}, J_{B2}, and J_{C2} were reversed. Taking the reverse-connection defect of the cable joint J_{A1} as an example for analysis, its equivalent circuit diagram was shown in Figure 5.
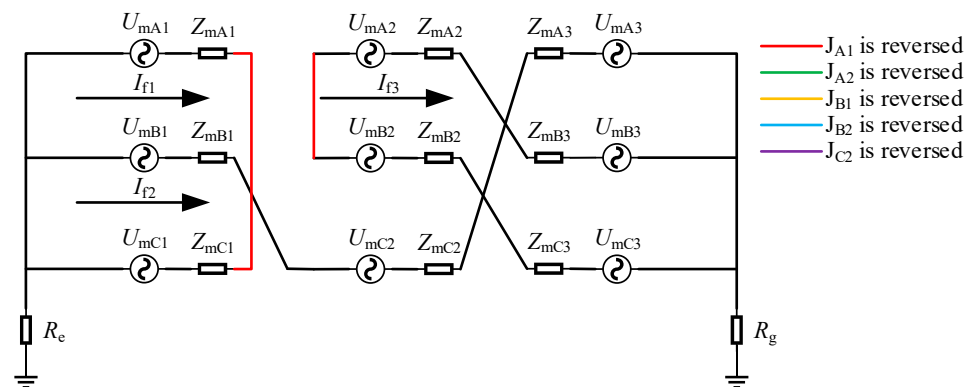
Figure 5. Equivalent circuit diagram when J_{A1} is reversed.

When the J_{A1} had a reverse-connection defect, the sheath circuit changed. There were three circuits in total. Loop 1 is A_1-C_1, loop 2 is B_1-C_2-A_3, and loop 3 is A_2-B_3-C_3-B_2. The induced current in the sheath would also change accordingly, as shown in Equation (9). The induced sheath current of loop 2 was consistent with that during normal operation and

its magnitude was close to 0. Since the impedance of loop 3 was $4Z_m$ and the impedance of loop 1 was $2Z_m$, the induced current of loop 1 was twice that of loop 3.

$$\begin{cases} I_{f1} = \frac{U_{mA1}-U_{mC1}}{Z_{mA1}+Z_{mC1}} \\ I_{f2} = I_{m2} \\ I_{f3} = \frac{U_{mA2}+U_{mB3}-U_{mC3}-U_{mB2}}{Z_{mA2}+Z_{mB3}+Z_{mC3}+Z_{mB2}} \end{cases} \tag{9}$$

where I_{f1}, I_{f2}, and I_{f3} were the induced currents in the sheath circuits under the current defect condition.

It could be seen from Figure 5 that the impedances of loops 1 and 3 had changed, so the distribution of the leakage current in each section of these two circuits would also change accordingly. Taking minor section A1 as an example, the change in its leakage current component was shown in Equation (10) (the leakage current components of each small section in other reverse-connection defects could be written using the current distribution rule, so no further analysis was carried out). Since loop 2 had not changed, its sheath current could still be obtained by Equation (8). Based on the above equations, the current in the grounding box could be obtained as shown in Equation (11). Since the leakage current was smaller than the induced current, the sheath current magnitude could be judged by the change in induced current. Among them, I_{la1} and I_{lc1} were at the two ends of the same sheath loop, so their magnitudes and phases were approximately the same. Similarly, it could be obtained that I_{lb2} and I_{lc2} were also approximately equal, and I_{lb1} and I_{la2} were also approximately equal. Obviously, at this time, I_{lb1} and I_{la2} were close to the current values during normal operation and were much smaller than the other four values, while I_{la1} and I_{lc1} would be greater than I_{lb2} and I_{lc2}.

$$\begin{cases} I_{LA1} = \frac{Z_{mRA1}+Z_{mC1}}{Z_{mA1}+Z_{mC1}} I_{A1} \\ I_{RA1} = \frac{Z_{mLA1}}{Z_{mA1}+Z_{mC1}} I_{A1} \end{cases} \tag{10}$$

$$\begin{cases} I_{la1} = -(I_{LA1} + I_{RC1}) + I_{f1} \\ I_{lb1} = -(I_{LB1} + I_{LC2} + I_{LA3}) + I_{f2} \\ I_{lc1} = -(I_{LC1} + I_{RA1}) - I_{f1} \\ I_{la2} = (I_{RB1} + I_{RC2} + I_{RA3}) + I_{f2} \\ I_{lb2} = (I_{RA2} + I_{RB3} + I_{LB2} + I_{LC3}) + I_{f3} \\ I_{lc2} = (I_{LA2} + I_{LB3} + I_{RB2} + I_{RC3}) - I_{f3} \end{cases} \tag{11}$$

3.2. Two Reversals

There were three categories of defects in which the inner core and outer shielding layer of the coaxial cable were reversed at two positions: reversed connections within the same cross-bonded link box, reversed connections of the same phase, and reversed connections at joints across different phases and cross-bonded link boxes.

3.2.1. Reversed Connections Within the Same Cross-Bonded Link Box

There was a total of six cases where two reversed connections of the inner core and outer shielding layer of the coaxial cable were located within the same cross-bonded link box: J_{A1} and J_{B1} were reversed simultaneously, J_{A1} and J_{C1} were reversed simultaneously, J_{B1} and J_{C1} were reversed simultaneously, J_{A2} and J_{B2} were reversed simultaneously, J_{A2} and J_{C2} were reversed simultaneously, and J_{B2} and J_{C2} were reversed simultaneously. Taking the case where J_{A1} and J_{B1} were reversed simultaneously as an example for analysis, the equivalent circuit diagram of this situation was shown in Figure 6.
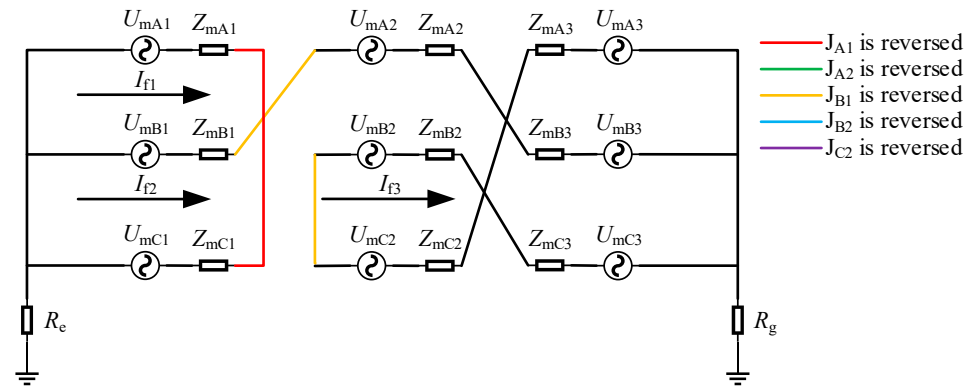
Figure 6. Equivalent circuit diagram when J_{A1} and J_{B1} are reversed.

When J_{A1} and J_{B1} were reversed simultaneously, there were three sheath loops: loop 1 was A_1-C_1, loop 2 was B_1-A_2-B_3, and loop 3 was B_2-C_3-A_3-C_2. Since the sheath circuits were inconsistent with those in normal operation, both the induced current in the sheath and the leakage current would change. It could be obtained from Figure 6 that the induced current in the sheath of the faulty circuit was as follows:

$$\begin{cases} I_{f1} = \frac{U_{mA1}-U_{mC1}}{Z_{mA1}+Z_{mC1}} \\ I_{f2} = \frac{U_{mB1}+U_{mA2}+U_{mB3}}{Z_{mB1}+Z_{mA2}+Z_{mB3}+R_e+R_g} \\ I_{f3} = \frac{U_{mB2}+U_{mC3}-U_{mA3}-U_{mC2}}{Z_{mB2}+Z_{mC3}+Z_{mA3}+Z_{mC2}} \end{cases} \tag{12}$$

There was a grounding resistance in loop 2, and the grounding resistance was much larger than the equivalent impedance of the sheath. Therefore, I_{f2} was the smallest. The impedance of loop 1 was twice that of loop 3, so the magnitude of I_{f1} was twice that of I_{f3}, and there was a 120° phase difference between them.

According to the superposition theorem, the current in the grounding box was as follows:

$$\begin{cases} I_{la1} = -(I_{LA1} + I_{RC1}) + I_{f1} \\ I_{lb1} = -(I_{LB1} + I_{LA2} + I_{LB3}) + I_{f2} \\ I_{lc1} = -(I_{LC1} + I_{RA1}) - I_{f1} \\ I_{la2} = (I_{LB2} + I_{LC3} + I_{RA3} + I_{RC2}) - I_{f3} \\ I_{lb2} = (I_{RB1} + I_{RA2} + I_{RB3}) + I_{f2} \\ I_{lc2} = (I_{RB2} + I_{RC3} + I_{LA3} + I_{LC2}) + I_{f3} \end{cases} \tag{13}$$

As shown in Figure 6, I_{la1} and I_{lc1} were located at the two ends of loop 1, so they were approximately equal. Similarly, it could be obtained that I_{lb1} and I_{lb2} were also approximately equal, and I_{la2} and I_{lc2} were also approximately equal. Judging from the magnitude relationship of the induced currents: I_{lb1} and I_{lb2} were greater than the current values during normal operation but smaller than the other four sheath currents. I_{la1} and I_{lc1} were the largest among the sheath currents at this time and were approximately equal to the corresponding current values when J_{A1} was reversed. Due to the influence of leakage current, the phase difference between I_{la1} and I_{lc2}, as well as between I_{la2} and I_{lc1}, was not 120°.

3.2.2. Reversed Connections of the Same Phase

There was a total of three cases where the two reversed connections of the inner core and outer shielding layer of the coaxial cable were of the same phase: J_{A1} and J_{A2} were reversed, J_{B1} and J_{B2} were reversed, and J_{C1} and J_{C2} were reversed. Taking the case where J_{A1} and J_{A2} were reversed as an example for introduction, the equivalent circuit diagram of this situation was shown in Figure 7.
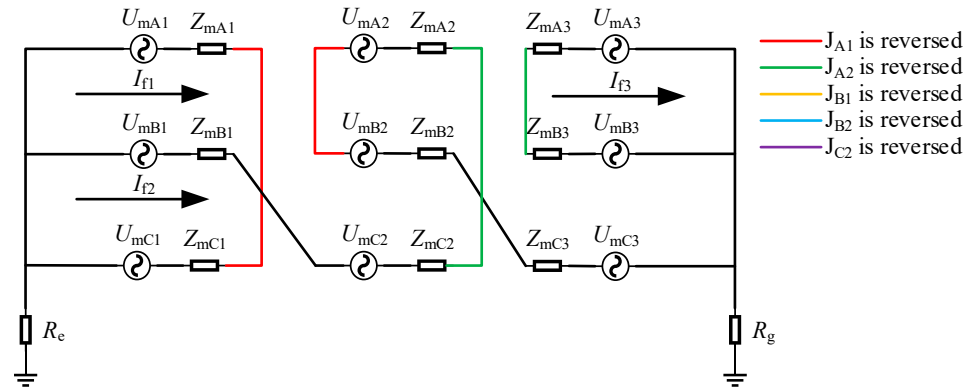
Figure 7. Equivalent circuit diagram when J_{A1} and J_{A2} are reversed.

When J_{A1} and J_{A2} were reversed simultaneously, the sheath circuit was different from that in normal operation. Loop 1 was A_1-C_1, loop 2 was B_1-C_2-A_2-B_2-C_3, and loop 3 was A_3-B_3. The induced current in the sheath of the corresponding circuit and the leakage current of each minor section of the metal sheath also changed accordingly. It could be obtained from Figure 7 that the induced current in the sheath of the faulty circuit was as follows:

$$\begin{cases} I_{f1} = \frac{U_{mA1}-U_{mC1}}{Z_{mA1}+Z_{mC1}} \\ I_{f2} = \frac{U_{mB1}+U_{mC2}-U_{mA2}+U_{mB2}+U_{mC3}}{Z_{mB1}+Z_{mC2}+Z_{mA2}+Z_{mB2}+Z_{mC3}+R_e+R_g} \\ I_{f3} = \frac{U_{mA3}-U_{mB3}}{Z_{mA3}+Z_{mB3}} \end{cases}, \tag{14}$$

As could be seen from Equation (14), the impedances of loops 1–3 were $2Z_m$, $5Z_m + R_e + R_g$, and $2Z_m$, respectively. Since the grounding resistance was much larger than the sheath impedance, the current of loop 2 was much smaller than that of the other loops. However, at this time, I_{f2} was slightly larger than the induced current value of loop 2 when J_{A1} and J_{B1} were reversed, while the magnitudes of I_{f1} and I_{f3} were equal.

According to the superposition theorem, the current in the grounding box was as follows:

$$\begin{cases} I_{la1} = -(I_{LA1} + I_{RC1}) + I_{f1} \\ I_{lb1} = -(I_{LB1} + I_{LC2} + I_{RA2} + I_{LB2} + I_{LC3}) + I_{f2} \\ I_{lc1} = -(I_{LC1} + I_{RA1}) - I_{f1} \\ I_{la2} = (I_{RA3} + I_{LB2}) + I_{f3} \\ I_{lb2} = (I_{LA3} + I_{RB3}) - I_{f3} \\ I_{lc2} = (I_{RB1} + I_{RC2} + I_{LA2} + I_{RB2} + I_{RC3}) + I_{f2} \end{cases} \tag{15}$$

Since the topology of loop 1 was consistent with that of loop 1 when J_{A1} and J_{B1} were reversed, and the topology of loop 3 was similar to it as well, the sheath currents were approximately equal. However, loop 2 had undergone significant changes and contained five minor sections of the metal sheath. Judging from the relationship of the induced sheath currents, the magnitudes of I_{la1}, I_{lc1}, I_{la2}, and I_{lb2} were approximately equal, while the current values of I_{lb1} and I_{lc2} were the smallest.

3.2.3. Reversed Connections at Joints Across Different Phases and Cross-Bonded Grounding Boxes

There was a total of six cases where the two reversed connections of the inner core and outer shielding layer of the coaxial cable were located at joints across different phases and cross-bonded grounding boxes: J_{A1} and J_{B2} were reversed simultaneously, J_{A1} and J_{C2} were reversed simultaneously, J_{B1} and J_{A2} were reversed simultaneously, J_{B1} and J_{C2} were reversed simultaneously, J_{C1} and J_{A2} were reversed simultaneously, and J_{C1} and J_{B2} were reversed simultaneously. According to the reversed topology, it could be further divided

into two cases. One case was that J_{A1} and J_{B2} are reversed simultaneously, J_{B1} and J_{C2} were reversed simultaneously, and J_{C1} and J_{A2} were reversed simultaneously. The other case was that J_{B1} and J_{A2} were reversed simultaneously, J_{C1} and J_{B2} were reversed simultaneously, and J_{A1} and J_{C2} were reversed simultaneously.

Take the simultaneous reversal of J_{A1} and J_{B2} as an example for the first case. The equivalent circuit diagram under this circumstance was shown in Figure 8.
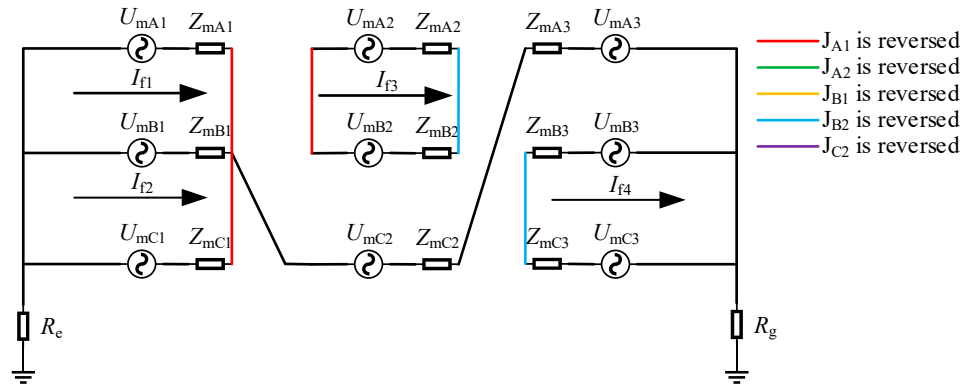
Figure 8. Equivalent circuit diagram when J_{A1} and J_{B2} are reversed.

When J_{A1} and J_{B2} were reversed simultaneously, there are four sheath loops: loop 1 was A_1-C_1, loop 2 was B_1-C_2-A_3, loop 3 was A_2-B_2, and loop 4 was B_3-C_3. Since loop 2 operated as in normal conditions, the induced current and leakage current in loop 2 remained unchanged, while those in other sheath circuits varied. It could be obtained from Figure 8 that the induced current in the sheath of the faulty circuit was as follows:

$$\begin{cases} I_{f1} = \frac{U_{mA1}-U_{mC1}}{Z_{mA1}+Z_{mC1}} \\ I_{f2} = \frac{U_{mB1}+U_{mC2}+U_{mA3}}{Z_{mB1}+Z_{mC2}+Z_{mA3}+R_e+R_g} \\ I_{f3} = \frac{U_{mA2}-U_{mB2}}{Z_{mA2}+Z_{mB2}} \\ I_{f4} = \frac{U_{mB3}-U_{mC3}}{Z_{mB3}+Z_{mC3}} \end{cases} \tag{16}$$

Loop 2 eliminated the induced voltage through a three-phase superposition. The voltages and impedances of the remaining loops were consistent. Therefore, the induced current of loop 2 was zero, and the magnitudes of the induced currents of the remaining loops were equal.

According to the superposition theorem, the current in the grounding box was as follows:

$$\begin{cases} I_{la1} = -(I_{LA1} + I_{RC1}) + I_{f1} \\ I_{lb1} = -(I_{LB1} + I_{LC2} + I_{LA3}) + I_{f2} \\ I_{lc1} = -(I_{LC1} + I_{RA1}) - I_{f1} \\ I_{la2} = (I_{RB1} + I_{RC2} + I_{RA3}) + I_{f2} \\ I_{lb2} = (I_{RB3} + I_{LC3}) + I_{f4} \\ I_{lc2} = (I_{LB3} + I_{RC3}) - I_{f4} \end{cases} \tag{17}$$

As could be seen from Figure 9, I_{la1} and I_{lc1} were located at the two ends of loop 1, so they were approximately equal. Similarly, it could be obtained that I_{lb1} and I_{la2} were also approximately equal, and I_{lb2} and I_{lc2} were also approximately equal. Loop 3 did not pass through the grounding box, so the current of this loop was not analyzed. Since the induced current value of loop 2 was zero, its sheath current was only the leakage current. It could be known that I_{lb1} and I_{la2} were close to zero. The magnitudes of the induced currents of loop 1 and loop 4 were equal, so the magnitudes of I_{la1}, I_{lc1}, I_{lb2}, and I_{lc2} were also approximately equal.
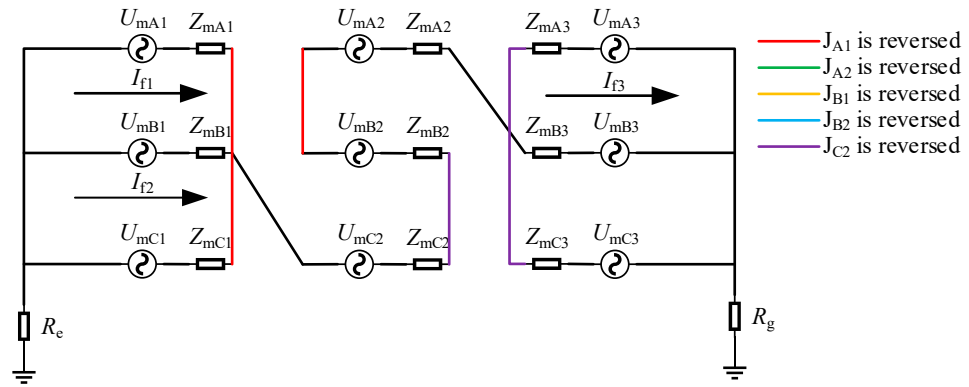
Figure 9. Equivalent circuit diagram when J_{A1} and J_{C2} are reversed.

Another case was analyzed by taking the simultaneous reversal of J_{A1} and J_{C2} as an example. The equivalent circuit diagram under this circumstance was shown in Figure 9.

When J_{A1} and J_{C2} were reversed simultaneously, there were three sheath loops in total. Loop 1 was A_1-C_1, loop 2 was B_1-C_2-B_2-A_2-B_3, and loop 3 was A_3-C_2. Loop 2 contained five minor sections of the metal sheath, and both the beginning and the end of loop 2 were of the B phase. The topologies of loop 1 and loop 3 were consistent, both containing the metal sheaths of phases A and C. As could be obtained from Figure 9, the induced sheath currents of the loops were as follows:

$$\begin{cases} I_{f1} = \frac{U_{mA1} - U_{mC1}}{Z_{mA1} + Z_{mC1}} = \frac{\sqrt{3}U_m \times e^{-j30^\circ}}{2Z_m} \\ I_{f2} = \frac{U_{mB1} + U_{mC2} - U_{mB2} + U_{mA2} + U_{mB3}}{Z_{mB1} + Z_{mC2} + Z_{mB2} + Z_{mA2} + Z_{mB3} + R_e + R_g} = 0 \\ I_{f3} = \frac{U_{mA3} - U_{mC3}}{Z_{mA3} + Z_{mC3}} = \frac{\sqrt{3}U_m \times e^{-j30^\circ}}{2Z_m} \end{cases} \tag{18}$$

As could be known from the above equation, loop 2 eliminated the induced voltage through voltage superposition, thus resulting in its induced current being zero. The induced currents of loop 1 and loop 3 were equal.

$$\begin{cases} I_{la1} = -(I_{LA1} + I_{RC1}) + I_{f1} \\ I_{lb1} = -(I_{LB1} + I_{LC2} + I_{RB2} + I_{LA2} + I_{LB3}) + I_{f2} \\ I_{lc1} = -(I_{LC1} + I_{RA1}) - I_{f1} \\ I_{la2} = (I_{RA3} + I_{LC3}) + I_{f3} \\ I_{lb2} = (I_{RB1} + I_{RC2} + I_{LB2} + I_{RA2} + I_{RB3}) + I_{f2} \\ I_{lc2} = (I_{LA3} + I_{RC3}) - I_{f3} \end{cases} \tag{19}$$

As could be seen from Figure 9 and Equation (19), I_{la1} and I_{lc1} were located at the two ends of loop 1, while I_{la2} and I_{lc2} were at the two ends of loop 3. The currents at the corresponding beginning and end of the two loops were basically equal. Since the induced current of loop 2 was zero, its sheath current, that is, leakage current, was close to zero and nearly identical to the current magnitude during normal operation.

Although these two reversed-connection cases both occurred in different phases and different cross-bonded grounding boxes, one had four loops while the other had three loops. In both reversed-connection cases, the sheath currents of two loops were basically equal, and the circulating current of the other loop was normal. However, the loop topologies of the two were not completely consistent.

3.3. Selection of Feature Quantities

Different reverse-connection defects in the cross-bonded grounding system significantly altered the metal sheath circuit compared to normal operation, thereby affecting

the sheath current in the grounding boxes at both ends. Therefore, we could use the sheath current as a feature to judge the operating state of the HV cable. The sheath current included two signals: amplitude and phase. However, in engineering practice, the measurement of the amplitude signal was relatively simple, and the data processing was more straightforward. In contrast, the phase signal was susceptible to electromagnetic interference, and its measurement was more difficult. Moreover, at present, the staff mainly rely on the amplitude signal of the sheath current to determine whether a fault occurs in the cable grounding system. Considering these practical factors, the current phase signal was excluded, and the feature quantities were constructed based solely on the amplitude signal to reflect the sheath circuit's operating state.

As could be known from the above analysis, during normal operation, the sheath currents I_{la1} and I_{lc2} jointly reflected the operating state of loop A_1-B_2-C_3, I_{lb1} and I_{la2} jointly reflected the operating state of loop B_1-C_2-A_3, and I_{lc1} and I_{lb2} jointly reflected the operating state of loop C_1-A_2-B_3. During the reversed operation, the sheath loops changed, and I_{la1}, I_{lc2}, I_{lb1}, I_{la2}, I_{lc1}, and I_{lb2} might not necessarily reflect the operating state of the same loop anymore. Therefore, feature quantities could be constructed based on the amplitudes of the above six currents. To reduce the influence of the cable operating voltage and parameters, the cable ratios were selected as the feature quantities, as shown in Equation (20).

Since the sheath currents I_{la1} and I_{lc2} jointly reflected the operating state of the loop A_1-B_2-C_3, I_{lb1} and I_{la2} jointly reflected the operating state of the loop B_1-C_2-A_3, and I_{lc1} and I_{lb2} jointly reflected the operating state of the loop C_1-A_2-B_3; the feature quantity could be constructed based on the amplitudes of the above six currents, as shown in Equation (20).

$$\begin{cases} t_1 = \left| \dfrac{I_{lc2} - I_{la1}}{\max(I_{la1}, I_{lc2})} \right|, \ t_2 = \left| \dfrac{I_{la2} - I_{lb1}}{\max(I_{la2}, I_{lb1})} \right|, \ t_3 = \left| \dfrac{I_{lb2} - I_{lc1}}{\max(I_{lc1}, I_{lb2})} \right| \\ t_4 = \dfrac{I_{la1}}{I_{lb1}}, \ t_5 = \dfrac{I_{lb1}}{I_{lc1}}, \ t_6 = \dfrac{I_{la1}}{I_{lc1}} \end{cases} \tag{20}$$

where t_1, t_2, and t_3 were the absolute values of the ratio of the amplitude difference of the same sheath circuit to the maximum amplitude of the circuit, which could reflect the operating state of the same metal sheath circuit. t_4, t_5, and t_6 were the amplitude ratios of the sheath current in the grounding box at the front end, which could reflect the operating state of different metal sheath circuits. According to the changes in the above six feature quantities, the type and location of the cable reverse-connection defect could be determined.

Thus, the feature quantity matrix used in this paper to reflect the operating state of the HV cable was as follows:

$$[t_1, t_2, t_3, t_4, t_5, t_6] \tag{21}$$

4. Simulation Analysis

In this paper, the cable of type YJLW03-64/110-1×800 was chosen for constructing the simulation model. The cables were arranged horizontally, with a burial depth of 1 m and a spacing of 0.27 m, spanning a total length of 1500 m. The three interconnected segments of the cross-bonded system each had a length of 500 m. The specific parameters are shown in Table 2 [24]. In the PSCAD v4.6.2 software, the cable line was modeled using a frequency-dependent model. The voltage level was set at 110 kV, and a three-phase balanced load was configured as a resistive load with a resistance value of 500 Ω. Meanwhile, the grounding resistance of the sheath circuit was 1 Ω. The simulation model built using PSCAD v4.6.2 software was shown in Figure 10.

Table 2. Simulation parameters of cable [24].

Cable Parameters	Value
Outer diameter of conductor/mm	34.2
Inner diameter of metal sheath/mm	78.6
Outer diameter of metal sheath/mm	82.6
Thickness of semiconductor shielding layer/mm	2
Thickness of insulation layer/mm	16
Outer diameter of cable/mm	94
Relative dielectric constant of XLPE	2.3
Resistivity coefficient of conductor/$(n\Omega \cdot m^{-1})$	16.8
Resistivity coefficient of the earth/$(\Omega \cdot m^{-1})$	100
Resistivity coefficient of sheath/$(n\Omega \cdot m^{-1})$	28.4
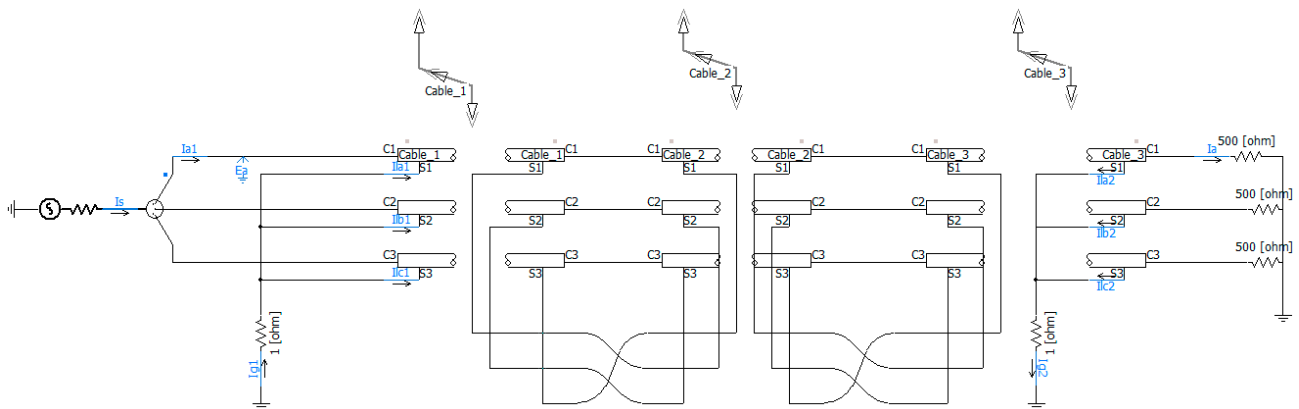
Figure 10. Simulation model.

4.1. Simulation of Cable in Normal Operation

According to the ammeter in the simulation model, the conductor current of the cable was 126.875 A. The simulation time was set to 0.3 s. When the cable was in normal operation, the waveforms of the sheath current in the grounding boxes at both ends were shown in Figure 11.
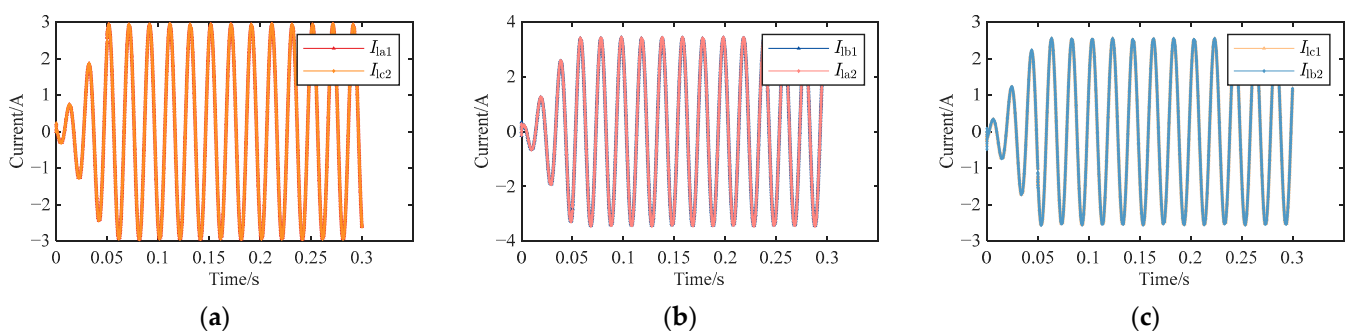
Figure 11. Waveform diagram of sheath current when the cable is in normal operation: (**a**) I_{la1} and I_{lc2}; (**b**) I_{lb1} and I_{la2}; and (**c**) I_{lc1} and I_{lb2}.

It could be seen from Figure 11 that, when the cable was in normal operation, the sheath currents in the grounding boxes at both ends of each sheath circuit were almost the same. The slight differences in the currents of different sheath circuits were due to the electromagnetic induction phenomenon between the conductor and the sheath. According to the oscilloscope in the simulation model, the sheath currents in the grounding boxes at both ends of different sheath circuits were measured as follows: $I_{la1} = 2.0883\angle152.3°$ A, $I_{lc2} = 2.0832\angle152.1°$ A, $I_{lb1} = 2.433\angle35.68°$ A, $I_{la2} = 2.437\angle35.55°$ A, $I_{lc1} = 1.803\angle-61.86°$ A,

and $I_{lb2} = 1.805\angle - 61.77°$ A. The corresponding feature quantity matrix was [0.00244, 0.00164, 0.0011, 0.858, 1.349, 1.158].

4.2. Simulation of One-Reversal Operation

Taking the reverse connection of the inner core and outer shielding layer of the coaxial cable at cable joint J_{A1} as an example for simulation analysis, when the J_{A1} had a reverse-connection defect, the waveforms of the sheath current in the grounding boxes were shown in Figure 12.
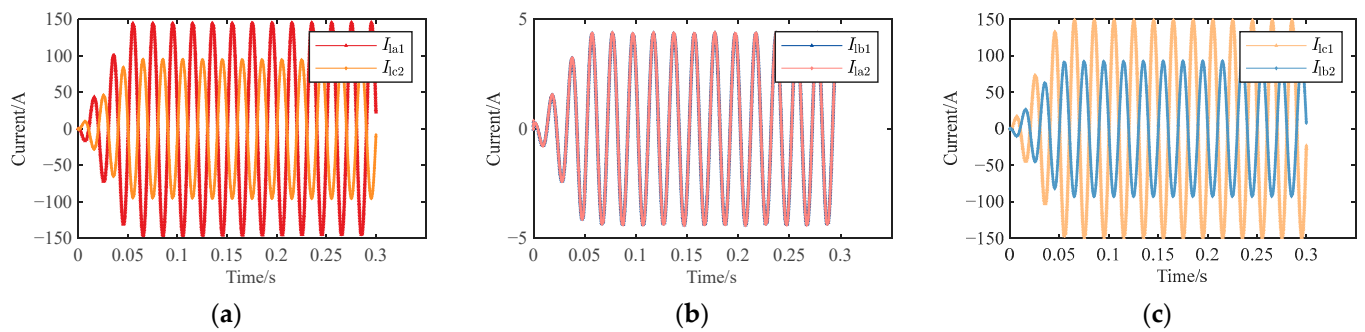
Figure 12. Waveform diagram of sheath current when J_{A1} is reversed: (**a**) I_{la1} and I_{lc2}; (**b**) I_{lb1} and I_{la2}; and (**c**) I_{lc1} and I_{lb2}.

Figure 12 showed that, when J_{A1} had a reverse-connection defect, the sheath currents in the grounding boxes at both ends of each sheath circuit changed significantly. However, the amplitudes and phases of I_{lb1} and I_{la2} were still approximately the same, because the sheath loop 2 was the same as that in normal operation. According to the oscilloscope in the simulation model, the sheath currents in the grounding boxes were measured as follows: $I_{la1} = 103.581\angle 81.75°$ A, $I_{lc2} = 67.219\angle - 94.67°$ A, $I_{lb1} = 3.10845\angle 49.91°$ A, $I_{la2} = 3.11119\angle 49.8°$ A, $I_{lc1} = 105.347\angle - 98.63°$ A, and $I_{lb2} = 65.512\angle 86.04°$ A. The corresponding feature quantity matrix was [0.351, 0.00088, 0.3781, 33.322, 0.0295, 0.9832].

Based on the above current values, the magnitudes of I_{la1} and I_{lc1} were nearly identical, with a phase difference of approximately 180°. The magnitudes of I_{lb1} and I_{la2} were basically the same as those during normal operation, and their phases were also basically equal. Since loop 3 contained four small sections of the metal sheath and loop 2 only contained two, the magnitudes of I_{lb2} and I_{lc2} were smaller compared to I_{la1} and I_{lc1}.

4.3. Simulation of Two-Reversal Operation

Taking the reverse connection of intermediate joints J_{A1} and J_{B1} as an example when the same cross-bonded grounding box was reversed, and taking the reverse connection of J_{A1} and J_{A2} as an example for the same-phase reverse connection, for the simulation of the reverse connection in different phases and different cross-bonded grounding boxes, the reverse connections of J_{A1} and J_{B2}, as well as J_{A1} and J_{C2}, were taken as examples. The waveforms of the sheath currents in the grounding box when these two joints were reversed were shown in Figure 13.

(a)

(b)

(c)

(d)
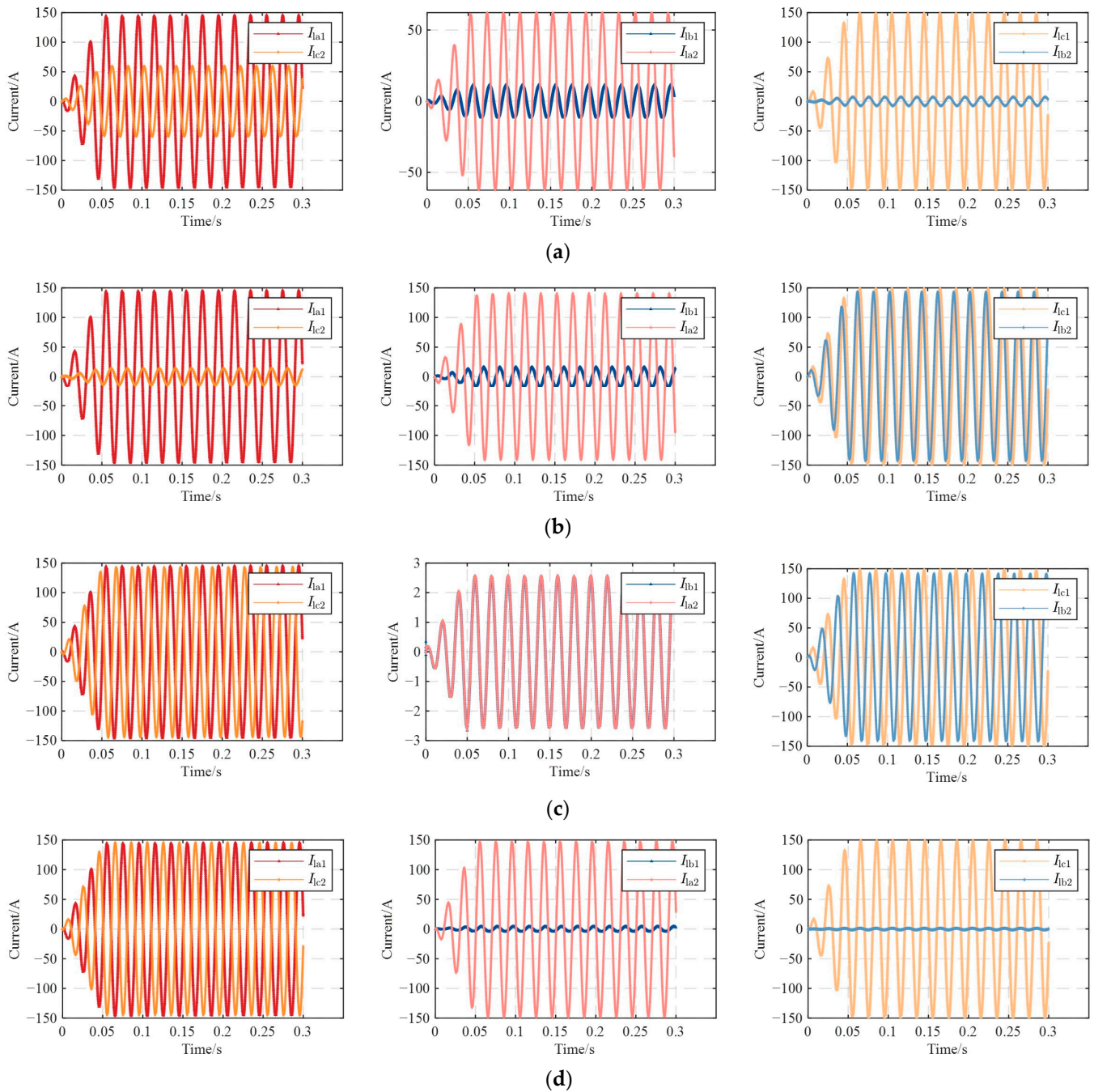
Figure 13. Waveform diagram of sheath current when the cable is in two-reversal operation: (**a**) J_{A1} and J_{B1} are reversed; (**b**) J_{A1} and J_{A2} are reversed; (**c**) J_{A1} and J_{B2} are reversed; and (**d**) J_{A1} and J_{C2} are reversed.

When J_{A1} and J_{B1} had a reverse connection, the sheath currents in the direct grounding boxes were measured as follows: $I_{la1} = 103.583\angle 81.75°$ A, $I_{lc2} = 42.16\angle -50.69°$ A, $I_{lb1} = 8.178\angle 72.15°$ A, $I_{la2} = 44.0269\angle 128.9°$ A, $I_{lc1} = 105.348\angle -98.64°$ A, and $I_{lb2} = 5.14868\angle 60.85°$ A. The corresponding feature quantity matrix was [0.59298, 0.8143, 0.9511, 12.666, 0.07763, 0.98325].

When J_{A1} and J_{A2} had a reverse connection, the sheath currents in the grounding boxes were measured as follows: $I_{la1} = 103.575\angle 81.75°$ A and $I_{lc2} = 9.84574\angle -28.24°$ A, $I_{lb1} = 11.5434\angle -23.82°$ A and $I_{la2} = 99.4441\angle 132.8°$ A, $I_{lc1} = 105.343\angle -98.64°$ A, and $I_{lb2} = 101.32\angle -47.48°$ A. The corresponding feature quantity matrix was [0.90494, 0.88392, 0.03838, 8.97266, 0.10958, 0.98322].

When J_{A1} and J_{B2} had reverse-connection defects, the sheath currents in the grounding boxes were measured as follows: $I_{la1} = 103.532\angle 81.71°$ A, $I_{lc2} = 102.003\angle - 143.2°$ A, $I_{lb1} = 1.82066\angle 10.29°$ A, $I_{la2} = 1.82713\angle 10.18°$ A, $I_{lc1} = 105.298\angle - 98.67°$ A, and $I_{lb2} = 100.494\angle 37.42°$ A. The corresponding feature quantity matrix was [0.014768, 0.003541, 0.045623, 56.8651, 0.017291, 0.98323].

When J_{A1} and J_{C2} had reverse-connection defects, the sheath currents in the grounding boxes were measured as follows: $I_{la1} = 103.581\angle 81.76°$ A, $I_{lc2} = 102.923\angle - 100.8°$ A, $I_{lb1} = 3.06403\angle 49.64°$ A, $I_{la2} = 104.717\angle 78.83°$ A, $I_{lc1} = 105.346\angle - 98.63°$ A, and $I_{lb2} = 0.95605\angle - 84.73°$ A. The corresponding feature quantity matrix was [0.006353, 0.97074, 0.9909, 33.8055, 0.02909, 0.98325].

When J_{A1} and J_{B1} were reversely connected, the loop 2 was B_1-A_2-B_3. Its induced voltage could not cancel each other out, so its amplitude was larger than that of the current during normal operation. Based on the measured current values, the amplitude of loop 2 was clearly larger than that during normal operation. Except for the reverse connection of J_{A1} and J_{C2}, loop 1 of the other three reverse-connection cases was the same as that of loop 1 when J_{A1} was reversed. It could be seen from the measured current values that the current of this loop was basically equal to that when J_{A1} was reversed. Since the loop topology in some reverse-connection cases was similar to that of loop 1, its current amplitude was also close to it. The amplitudes measured in loop 2 when J_{A1} and J_{B2} were reversely connected and when J_{A1} and J_{C2} were reversely connected were both close to those during normal operation.

4.4. Dataset Construction

Based on the above-built HV cable simulation model, simulations of different defect types were carried out. Under constant cable structure parameters, sheath current data were obtained by varying the cable length and load resistance. The feature quantity matrices reflecting the operating state of the HV cable were constructed according to Equations (20) and (21). The length of each section of the HV cable using the cross-bonded grounding method was generally 500 m. Therefore, the value range of each cable section's length was set from 400 m to 600 m, and then increased by 50 m successively, resulting in five selection methods. In actual power systems, the load resistance was determined by the equipment used by users. Hence, the value range of the load resistance was set from 500 Ω to 800 Ω, increasing by 50 Ω successively, which leads to seven selection methods. There were 35 parameter combinations for each defect location, and there were 21 defect locations in total. The dataset had 770 groups in total.

The selection of cable length and load resistance was based on the actual operation of HV cables. By designing a reasonable parameter range, both the diversity and representativeness of the simulation dataset were ensured, providing sufficient data support for subsequent defect diagnosis.

5. Reverse Defect Diagnosis Model

5.1. SVM Model

The SVM is a machine-learning algorithm used for regression and classification [25]. Its core idea is to find an optimal hyperplane to distinguish between different categories of data. By maximizing the margin, the robustness of the algorithm is improved, and it has significant advantages in dealing with problems such as small samples, nonlinearity, and overfitting.

SVM processes nonlinearly separable data through kernel functions. Common kernel functions include the linear kernel function, RBF kernel function, sigmoid kernel function, etc. Due to the excellent generalization ability and wide application of the radial basis

function (RBF) kernel function, this paper selects the RBF kernel function. At this time, the accuracy of the SVM model is greatly affected by the penalty factor C and the kernel function parameter g. Adjusting C affects the model's generalization ability and training speed, while g determines the kernel function's shape and complexity, influencing data mapping in high-dimensional space. To give the SVM model a better classification ability, appropriate parameters need to be selected to achieve the best effect.

5.2. Artificial Rabbits Optimization Algorithm

The artificial rabbits optimization algorithm was proposed by Liying Wang et al. in 2022 [26]. This algorithm originates from the survival strategies of rabbits in nature. These strategies mainly consist of detouring foraging and random hiding, which are exploration and exploitation, respectively. The switch between them is based on the energy contraction mechanism. To avoid predators detecting their burrow, rabbits forage randomly in areas distant from their burrow during the foraging process. This behavior greatly improves the exploration efficiency and global search ability of the algorithm. At each iteration of the ARO algorithm, each rabbit digs d burrows along each dimension of the search space and randomly selects one in which to hide, promoting search diversity through the random hiding strategy. In the initial stage of iteration, the rabbits in the population tend to detour foraging due to their relatively high energy. As the energy decreases, they will execute the random hiding strategy. In the ARO algorithm, when the energy factor A > 1, the rabbit is in the exploration stage; otherwise, it is in the exploitation stage. After implementing either the detouring foraging or the random hiding strategy, the position of the rabbit is called the candidate position. The actual position of the rabbit will change according to the fitness value between the candidate position and the current position. If the candidate position has better fitness, the rabbit will move to that position; otherwise, it will stay in its current position. The flowchart of the ARO algorithm is shown in Figure 14.

5.3. Defect Diagnosis Model Based on ARO-SVM

This paper used the ARO algorithm to optimize the SVM model. The specific diagnosis steps are as follows:

1. The acquisition and preprocessing of sheath current amplitude information. Simulate various defects using PSCAD v4.6.2 software, collect the sheath current amplitude data from the grounding boxes at both ends of the HV cable, and construct feature vectors based on Equations (20) and (21). The formed dataset is then randomly divided into a training set and a test set at a ratio of 4:1.

2. Model training. Firstly, the parameters of the ARO algorithm are initialized. Selecting an appropriate initial population size and maximum number of iterations is crucial to balancing the search accuracy and computational efficiency. The population size was set to 30, and the maximum number of iterations (t_{max}) was set to 50. The population size and iteration count should be adjusted based on whether the fitness function converges when the maximum iteration is reached. Select the population strategy based on the energy factor value and calculate the defect diagnosis accuracy after each parameter update. Update the optimal accuracy and parameters until the stopping condition is met and the maximum iterations are reached to obtain the optimal SVM model. Defect identification. Input the test set into the SVM model obtained in the previous step for defect identification.
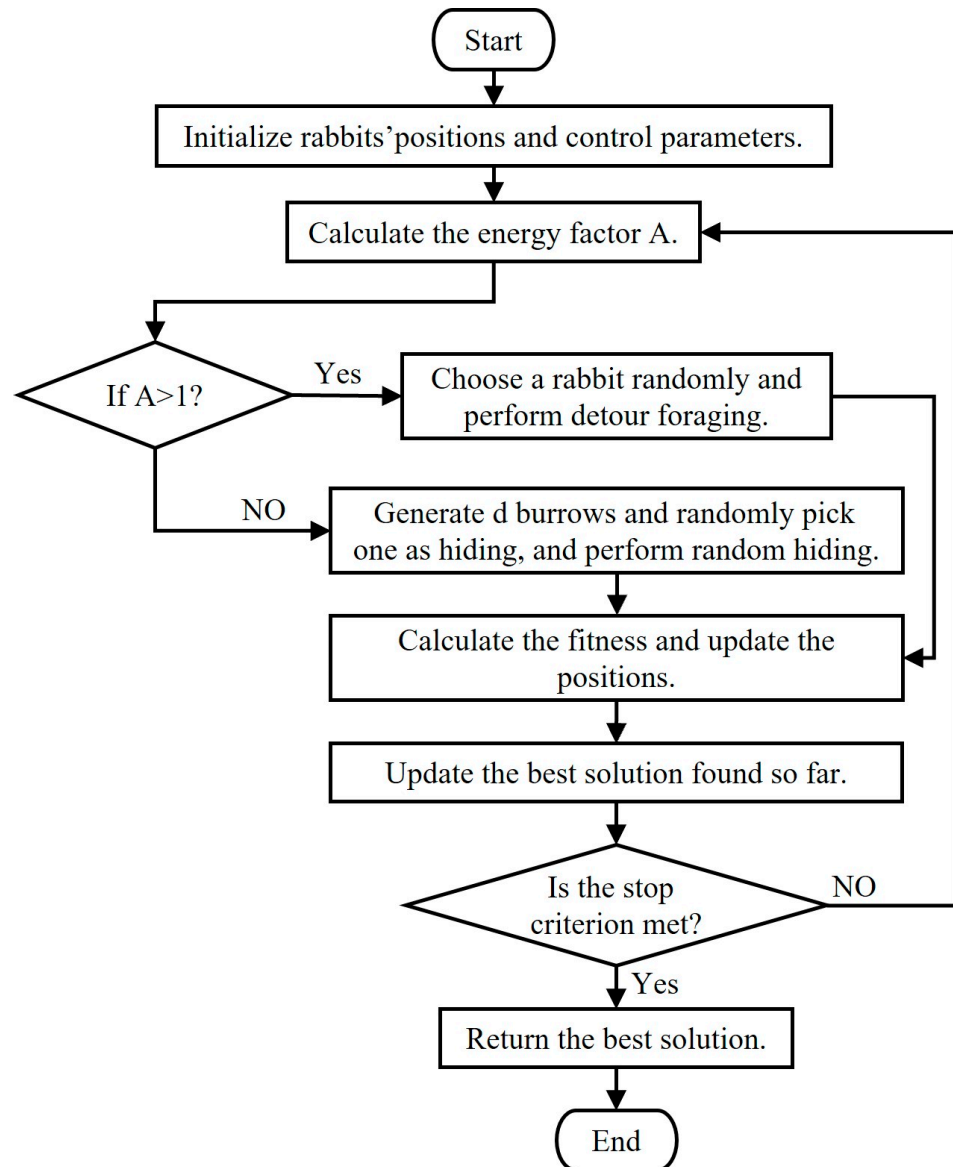
Figure 14. Flowchart of ARO algorithm [26].

　　　The flowchart of the defect diagnosis model based on ARO-SVM was shown in Figure 15.

　　　The optimization effect of the ARO-SVM model could be verified by comparing with the decision tree (DT), extreme gradient boosting (XGBoost), back propagation (BP), SVM, PSO-SVM, and SSA-SVM models through control experiments [27–31]. By inputting the same training set and test set, the defect diagnosis accuracy of each model could be obtained as shown in Table 3.

　　　As shown in Table 3, the defect diagnosis accuracies of the DT, XGBoost, BP, SVM, ARO-DT, ARO-XGBoost, ARO-BP, PSO-SVM, SSA-SVM, and ARO-SVM models were 92.86%, 98.05%, 90.26%, 93.51%, 97.40%, 98.70%, 91.56%, 98.05%, 95.45%, and 99.35%, respectively. The accuracy of the ARO-SVM model was increased by 6.49%, 1.3%, 9.09%, 5.84%, 1.95%, 0.65%, 7.79%, 1.3%, and 3.9% compared with those of the DT, XGBoost, BP, SVM, ARO-DT, ARO-XGBoost, ARO-BP, PSO-SVM, and SSA-SVM models, respectively. Since the ARO-SVM model exhibited the highest accuracy, this paper selected the ARO algorithm to optimize the SVM model. Compared with the SVM model, the ARO-SVM model could accurately identify the defects with state numbers 3, 4, and 6, and the accuracy of the defect with state number 2 was also 90.91%. Therefore, the algorithm proposed in this

paper can accurately identify the reverse-connection defects in the HV cable cross-bonded grounding system.
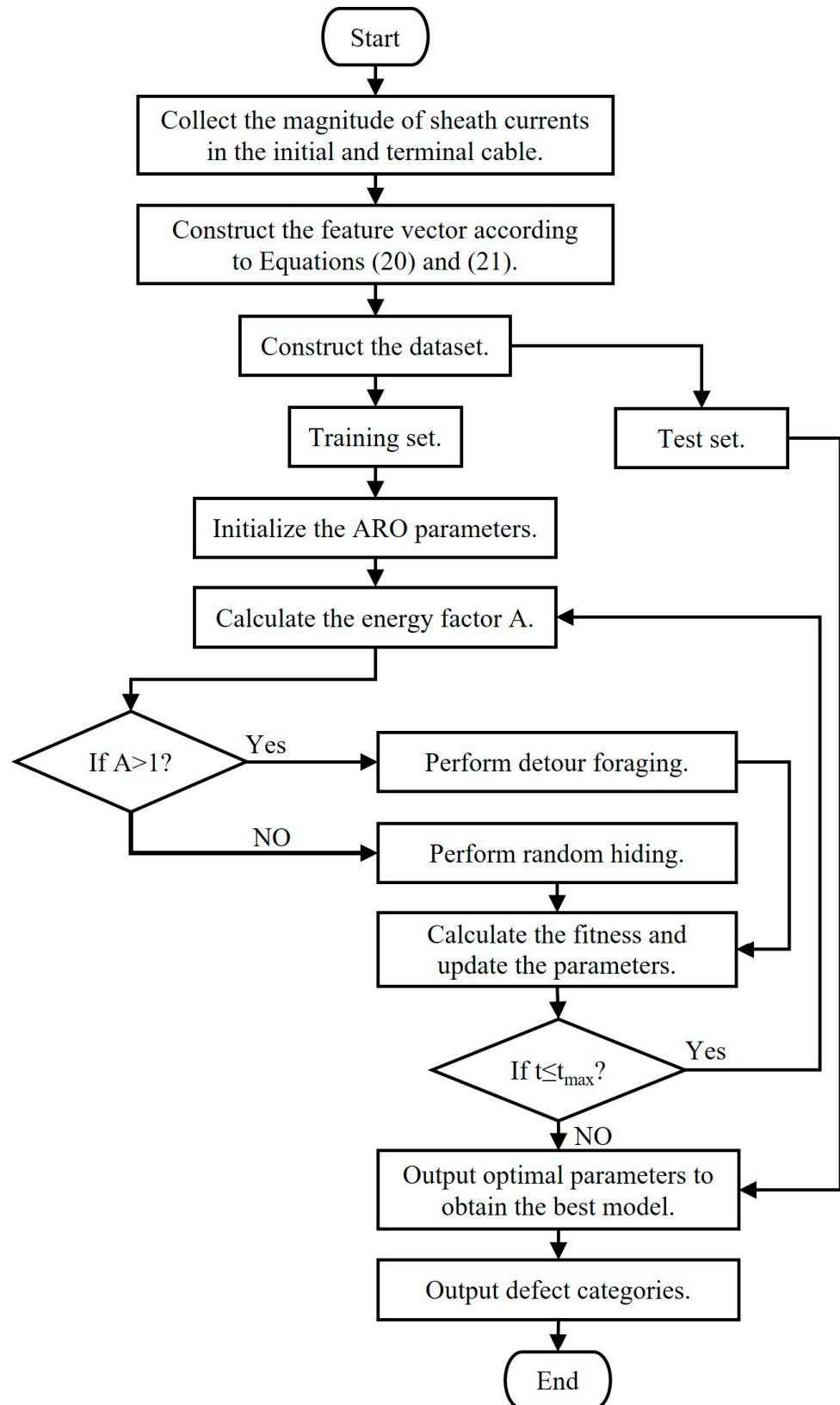
Figure 15. Flowchart of the defect diagnosis model based on ARO-SVM.

Table 3. Defect diagnosis accuracy of different models.

State Number	DT	XGBoost	BP	SVM	ARO-DT	ARO-XGBoost	ARO-BP	PSO-SVM	SSA-SVM	ARO-SVM
0	100%	100%	100%	100%	100%	100%	100%	100%	100%	100%
1	100%	100%	100%	100%	88.89%	100%	100%	100%	100%	100%
2	47.62%	100%	0%	77.78%	90.91%	100%	66.67%	100%	83.33%	90.91%
3	100%	100%	0%	0%	100%	100%	62.50%	100%	0%	100%
4	100%	100%	37.50%	37.50%	100%	100%	0%	50%	37.50%	100%
5	100%	100%	100%	100%	100%	100%	100%	100%	100%	100%
6	0%	100%	52.38%	75%	91.67%	100%	100%	100%	100%	100%
7	100%	100%	100%	100%	100%	100%	100%	100%	100%	100%
8	100%	75%	100%	100%	100%	85.71%	100%	100%	100%	100%
9	100%	100%	100%	100%	100%	100%	100%	100%	100%	100%
10	100%	88.89%	100%	100%	100%	100%	100%	100%	100%	100%
11	100%	100%	100%	100%	100%	100%	100%	100%	100%	100%
12	100%	100%	100%	100%	100%	100%	100%	100%	100%	100%
13	100%	100%	100%	100%	100%	100%	100%	100%	100%	100%
14	100%	100%	100%	100%	100%	100%	100%	100%	100%	100%
15	100%	100%	100%	100%	100%	100%	100%	100%	100%	100%
16	100%	100%	100%	100%	80%	100%	100%	100%	100%	100%
17	100%	100%	100%	100%	100%	87.50%	53.85%	100%	100%	100%
18	100%	100%	100%	100%	100%	100%	100%	100%	100%	100%
19	100%	100%	100%	100%	100%	100%	100%	100%	100%	100%
20	100%	100%	100%	100%	100%	100%	100%	100%	100%	100%
21	100%	100%	100%	100%	100%	100%	100%	100%	100%	100%
Accuracy	92.86%	98.05%	90.26%	93.51%	97.40%	98.70%	91.56%	98.05%	95.45%	99.35%

5.4. Influence of Noise Interference

In actual operation, noise interference distorted the sheath current waveform of the HV cable cross-bonded grounding system, affecting measurement accuracy. To test the model's robustness against noise, noise with SNRs of 20, 30, and 40 dB was added to the simulated sheath current waveform. The smaller the SNR, the stronger the noise signal. The feature vectors obtained after adding noise interference were input into the model, and various types of reverse-connection defects were tested. The specific test results were shown in Table 4.

Table 4 showed that, under noise interference with different SNRs, the model accurately identified defect types and demonstrated strong resistance to noise.

5.5. Case Verification

In this paper, a 220 kV HV cable line was taken as an example for analysis [32]. The total length of this cable line was 6.77 km, and it adopted the cross-bonded grounding method, including 2 GIS terminals and 11 intermediate joints. After a certain grounding circulating current measurement, the operators found that the data between box No. 9 and the GIS terminal were abnormal. The measured values of the sheath current were shown in Table 5.

According to the measured values of the sheath current, the actual wiring method causing the defect in the grounding system was shown in Figure 16. It could be clearly seen that the defect was the simultaneous reverse connection of the inner core and outer shielding layer at intermediate joints J_{A1} and J_{A2}. This state corresponded to the fault numbered 13 as defined in Table 1 of this paper. Calculate the sheath current feature matrix according to Equations (20) and (21) as [0.094506, 0.92391, 0.009365, 13, 0.07353, 0.95588]. Input it into the ARO-SVM model, and the diagnosis result was 13, which was the same as the actual state number. Therefore, the proposed model effectively diagnoses reverse-connection defects in HV cables and is unaffected by the operating voltage and cable structure parameters.

Table 4. Robustness test results.

Actual Operating State	Corresponding Number	SNR/dB	Test Results
Normal	0	20 30 40	0 0 0
Misconnection of joint J_{A1}	1	20 30 40	1 1 1
Misconnection of joint J_{A1} and J_{B1}	7	20 30 40	7 7 7
Misconnection of joint J_{A1} and J_{A2}	13	20 30 40	13 13 13
Misconnection of joint J_{A1} and J_{B2}	16	20 30 40	16 16 16
Misconnection of joint J_{A1} and J_{C2}	21	20 30 40	21 21 21

Table 5. Measured values of sheath current [32].

Location	Sheath Current of Phase A/A	Sheath Current of Phase B/A	Sheath Current of Phase C/A
Box No. 9	91.0	7.0	95.2
Box No. 10	6.8	8.3	83.9
Box No. 11	87.0	7.3	4.3
GIS terminal	92.0	96.1	5.0
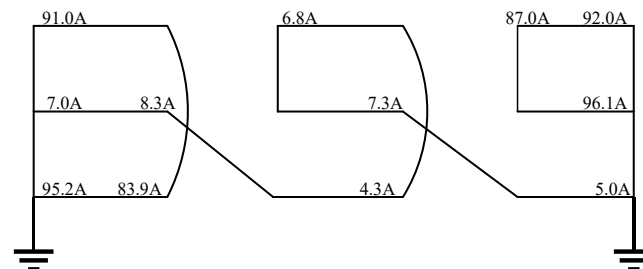
Figure 16. Actual wiring method.

Existing detection methods [33] can only determine whether a defect has occurred in the HV cable cross-bonded grounding system, but cannot accurately identify the type of defect. In contrast, the algorithm proposed in this paper not only accurately identifies reverse-connection defects in the grounding system but also roughly locates the defect position in the cable, significantly reducing the maintenance time for technicians.

5.6. Discussion on Practical Deployment and Challenges

According to the above analysis, the ARO-SVM-based cable reverse-connection defect diagnosis model effectively identifies defects in the sheath grounding system. However, in practical applications, we still need to consider the possible challenges that this model may face.

To integrate the proposed method with the existing HV cable cross-bonded grounding system, current transformers and data acquisition modules must be installed in the grounding boxes at both ends for online sheath current monitoring. Additionally, as the cable system expands, we must further optimize the ARO-SVM model to adapt to more

complex power system environments and maintain a high diagnostic accuracy. For the computational cost of the ARO-SVM model, future research could explore an improved version based on lightweight optimization algorithms to reduce the demand for hardware resources. Meanwhile, during deployment, real-time diagnosis through edge computing can reduce latency and improve overall system efficiency. The proposed model is applicable not only to diagnosing cable reverse-connection defects but also to detecting other defects in the HV cable cross-bonded grounding system. In future research, we also need to consider building a more comprehensive and multifunctional diagnostic model. During the actual operation process, the operators need to pay special attention to the following points: Firstly, before the cable line is put into operation, the correct installation and calibration of the current sensors must be ensured. During the cable line operation, the sensors and data acquisition modules should be regularly checked to ensure real-time data updates and validity. To effectively reduce cable reverse-connection defects, operators should also conduct comprehensive connectivity checks before cable installation.

In conclusion, the application of the cable reverse-connection defect diagnosis model based on ARO-SVM in the HV cable grounding system has high potential and can effectively identify reverse-connection defects and improve the reliability of the power system.

6. Conclusions

This paper proposed a method to judge cable reverse-connection defects by using the sheath current amplitude in the grounding boxes at both ends of the HV cable. An equivalent model of the HV cable cross-bonded grounding system was established, and defect diagnosis was carried out with the help of simulation and ARO-SVM models. The conclusions were as follows:

1. The amplitude of the sheath current will change with different reverse-connection defects. Based on this, different reverse-connection defects can be diagnosed.
2. The ARO algorithm was used to optimize the SVM model. The diagnostic accuracy rate of the ARO-SVM model for reverse-connection defects was increased by 6.49%, 1.3%, 9.09%, and 5.84%, respectively, compared with those of the DT, XGBoost, BP, and SVM models. It can be seen from this that the proposed algorithm can effectively diagnose the reverse-connection defects of HV cables.
3. The defects of the HV cable cross-bonded grounding system do not only include the reverse-connection defect. In future research, we will focus on constructing a model with more comprehensive fault identification capabilities.

Abbreviations

The following abbreviations are used in this manuscript:

HV High-Voltage
SVM Support Vector Machine
ARO Artificial Rabbits Optimization

References

1. Wang, E.; Chen, X.; Zhu, H.; Yin, K.; Awais, M.; Paramane, A. Steady-State Electrical Properties and Loss Reduction Measures Analysis for 220 kV Tunnel Cable System. *Electr. Power Syst. Res.* **2024**, *227*, 109957. [CrossRef]
2. Liu, J.; Ma, M.; Liu, X.; Xu, H. High-Voltage Cable Buffer Layer Ablation Fault Identification Based on Artificial Intelligence and Frequency Domain Impedance Spectroscopy. *Sensors* **2024**, *24*, 3067. [CrossRef] [PubMed]
3. Song, Y.; Chen, W.; Wan, F.; Zhang, Z.; Du, L.; Wang, P.; Li, J.; Wu, Z.; Huang, H. Online Multi-Parameter Sensing and Condition Assessment Technology for Power Cables: A Review. *Electr. Power Syst. Res.* **2022**, *210*, 108140. [CrossRef]
4. Lyu, C.; Wang, S.; Liu, S.; Guo, Y. Method for Measuring Interface Pressure of High-Voltage Cables. *Electronics* **2022**, *11*, 1419. [CrossRef]
5. Li, M.; Liu, J.; Zhu, T.; Zhou, W.; Zhou, C. A Novel Traveling-Wave-Based Method Improved by Unsupervised Learning for Fault Location of Power Cables via Sheath Current Monitoring. *Sensors* **2019**, *19*, 2083. [CrossRef]
6. Akbal, B. Multi-objective optimization and hybrid AI-based cable grounding method to prevent insulation failures in armored high voltage cables. *J. Fac. Eng. Archit. Gazi Univ.* **2024**, *39*, 1351–1364. [CrossRef]
7. Akbal, B. Applications of Artificial Intelligence and Hybrid Neural Network Methods with New Bonding Method to Prevent Electroshock Risk and Insulation Faults in High-Voltage Underground Cable Lines. *Neural Comput. Appl.* **2018**, *29*, 97–105. [CrossRef]
8. Li, R.-F.; Hu, H.; Cao, X.-B.; Li, Z.-M.; Li, J.-H.; Zhu, C.-L.; Liu, L.-J. A Novel Distributed Equivalent Circuit Model for Single-Core Cables. *J. Electr. Eng. Technol.* **2023**, *19*, 601–612. [CrossRef]
9. Wang, M.; Liu, Y.; Huang, Y.; Xin, Y.; Han, T.; Du, B. Defect Identification of XLPE Power Cable Using Harmonic Visualized Characteristics of Grounding Current. *Electronics* **2024**, *13*, 1159. [CrossRef]
10. Li, M.; Zhou, W.; Wang, C.; Yao, L.; Su, M.; Huang, X.; Zhou, C. A Novel Fault Localization Method Based on Monitoring of Sheath Current in a Cross-Bonded HV Cable System. In Proceedings of the 2017 IEEE Electrical Insulation Conference (EIC), Baltimore, MD, USA, 11–14 June 2017; IEEE: New York, NY, USA, 2017; pp. 123–126.
11. Dong, X.; Yang, Y.; Zhou, C.; Hepburn, D.M. Online Monitoring and Diagnosis of HV Cable Faults by Sheath System Currents. *IEEE Trans. Power Deliv.* **2017**, *32*, 2281–2290. [CrossRef]
12. Shokry, M.A.; Khamlichi, A.; Garnacho, F.; Malo, J.M.; Álvarez, F. Detection and Localization of Defects in Cable Sheath of Cross-Bonding Configuration by Sheath Currents. *IEEE Trans. Power Deliv.* **2019**, *34*, 1401–1411. [CrossRef]
13. Álvarez, F.; Garnacho, F.; Ortego, J.; Sánchez-Urán, M.Á. Application of HFCT and UHF Sensors in On-Line Partial Discharge Measurements for Insulation Diagnosis of High Voltage Equipment. *Sensors* **2015**, *15*, 7360–7387. [CrossRef] [PubMed]
14. Lan, X.; Zhou, N.; Liu, M.; Sun, T.; Wang, J.; Wang, Q. Identification of Defects in HV Cable Sheath Based on Equivalent Impedance Spectrum Characteristic Coding. *Int. J. Electr. Power Energy Syst.* **2021**, *130*, 107008. [CrossRef]
15. Li, M.; Zhou, C.; Zhou, W.; Wang, C.; Yao, L.; Su, M.; Huang, X. A Novel Fault Location Method for a Cross-Bonded HV Cable System Based on Sheath Current Monitoring. *Sensors* **2018**, *18*, 3356. [CrossRef]
16. Li, G.; Chen, J.; Li, H.; Hu, L.; Zhou, W.; Zhou, C. Detection of Irregular Sheath Current Distribution for Diagnosis of Faults in Grounding Systems of Cross-Bonded Cables. *IEEE Access* **2023**, *11*, 68453–68461. [CrossRef]
17. Zhu, B.; Yu, X.; Tian, L.; Wei, X. Insulation Monitoring and Diagnosis of Faults in Cross-Bonded Cables Based on the Resistive Current and Sheath Current. *IEEE Access* **2022**, *10*, 46057–46066. [CrossRef]
18. Wan, Q.; Yan, X. Fault Diagnosis of HV Cable Metal Sheath Grounding System Based on LSTM. *Appl. Sci.* **2023**, *13*, 2453. [CrossRef]
19. Pan, W.; Li, Y.; Sun, K.; Zhu, Z.; Li, X. Incipient Fault Location Method of Cable Based on Both-End Electric Quantities. *IEEE Access* **2020**, *8*, 219503–219512. [CrossRef]
20. Yao, S. Analysis of Energized Diagnosis of Defects in Cable Cross Connection System. *Wire Cable* **2022**, *2*, 37–42+46. [CrossRef]
21. Zhou, J.; Xiao, M.; Niu, Y.; Ji, G. Rolling Bearing Fault Diagnosis Based on WGWOA-VMD-SVM. *Sensors* **2022**, *22*, 6281. [CrossRef]
22. Zhang, S.; Zhou, H. Transformer Fault Diagnosis Based on Multi-Strategy Enhanced Dung Beetle Algorithm and Optimized SVM. *Energies* **2024**, *17*, 6296. [CrossRef]
23. Mahtani, K.; Granizo, R.; Guerrero, J.M.; Platero, C.A. Detection of Faulty Energizations in High Voltage Direct Current Power Cables by Analyzing Leakage Currents. *Electronics* **2024**, *13*, 4120. [CrossRef]

24. Yang, M.; Xia, C.; Lai, S.; Chi, Z. Fault Location of Cross-Connected Cables Based on Reactive Power Characteristics of Core-Sheath Transition Resistance. *Trans. China Electrotech. Soc.* **2024**, *39*, 137–1389.

25. Chauhan, V.K.; Dahiya, K.; Sharma, A. Problem Formulations and Solvers in Linear SVM: A Review. *Artif. Intell. Rev.* **2019**, *52*, 803–855. [CrossRef]

26. Wang, L.; Cao, Q.; Zhang, Z.; Mirjalili, S.; Zhao, W. Artificial Rabbits Optimization: A New Bio-Inspired Meta-Heuristic Algorithm for Solving Engineering Optimization Problems. *Eng. Appl. Artif. Intell.* **2022**, *114*, 105082. [CrossRef]

27. Costa, V.G.; Pedreira, C.E. Recent Advances in Decision Trees: An Updated Survey. *Artif. Intell. Rev.* **2023**, *56*, 4765–4800. [CrossRef]

28. Zhang, C.; Hu, D.; Yang, T. Anomaly Detection and Diagnosis for Wind Turbines Using Long Short-Term Memory-Based Stacked Denoising Autoencoders and XGBoost. *Reliab. Eng. Syst. Saf.* **2022**, *222*, 108445. [CrossRef]

29. Li, J.; Yao, X.; Wang, X.; Yu, Q.; Zhang, Y. Multiscale Local Features Learning Based on BP Neural Network for Rolling Bearing Intelligent Fault Diagnosis. *Measurement* **2020**, *153*, 107419. [CrossRef]

30. Qu, N.; Zuo, J.; Chen, J.; Li, Z. Series Arc Fault Detection of Indoor Power Distribution System Based on LVQ-NN and PSO-SVM. *IEEE Access* **2019**, *7*, 184020–184028. [CrossRef]

31. Qu, J.; Ma, X.; Wang, M.; Ma, B. Hybrid Fault Diagnosis Method Based on Wavelet Packet Energy Spectrum and SSA-SVM. *Int. J. Adv. Comput. Sci. Appl.* **2022**, *13*, 52–60. [CrossRef]

32. Yu, L.; Wei, Z.; Ding, B.; Chen, Y. Analysis of Circulation Current Abnormality Caused by Defects in Power Cable Grounding System. *Shandong Electr. Power* **2020**, *47*, 26–29.

33. State Grid Corporation of China. *Q GDW 11223-2014: Technical Specification for State Detection of HV Cable Lines*; State Grid Corporation of China: Beijing, China, 2014.